processes

MDPI

Article

Modeling and Simulation of a Real Lime Kiln Plant to Understand Ring Formation Phenomena

Rui Neves-Silva [1,*], Paulo Pina [2] and Joaquim Belfo [3]

[1] School of Science and Technology and Uninova CTS, NOVA University of Lisbon, Campus de Caparica, 2829-516 Caparica, Portugal
[2] inknow solutions, 1600-312 Lisboa, Portugal; pina@inknow.pt
[3] The Navigator Company, 2901-861 Setúbal, Portugal
* Correspondence: rns@fct.unl.pt

Abstract: This paper presents a study on the ring formation phenomenon in lime kilns using simulation. The research focuses on the chemical recovery cycle integrated into the pulp production process at a pulp mill, with particular emphasis on the calcium cycle within the lime kilns. Lime kilns are critical components, as their unavailability can significantly impact the overall cost-effectiveness of the facility. The calcination of lime sludge occurs in a rotary kiln, where calcium carbonate in the lime sludge is converted into calcium oxide (lime). Under certain conditions, material can progressively accumulate, leading to ring formation and eventual kiln clogging, resulting in operational downtime. To investigate this issue, the authors developed a physics-based model using a finite-dimensional, one-dimensional approach that considers only longitudinal variation. Several approximations were made to maintain a reasonable simulation time without compromising accuracy. Simulations based on real operational data identified fluctuations in fuel flow rate and sulfur content from non-condensable gases as key contributors to ring formation. The results showed that these fluctuations caused instability in the temperature profiles of the solids and gas beds, leading to periods of cooling before the lime sludge reaches the outlet to the coolers. This cooling promotes the recarbonation of lime and, consequently, the formation of rings. The findings highlight that stabilizing fuel flow and managing sulfur content could mitigate ring formation and improve kiln efficiency. The developed model provides a valuable tool for predictive analysis and process optimization, potentially supporting the development of a digital twin to enhance real-time monitoring and operational control.

Keywords: ring formation; lime kiln; physics-based modelling; finite-dimensional modelling; simulation of industrial plants

Academic Editors: Gabriella Bognár and Krisztian Hriczo

Received: 28 January 2025
Revised: 13 March 2025
Accepted: 26 March 2025
Published: 29 March 2025

Citation: Neves-Silva, R.; Pina, P.; Belfo, J. Modeling and Simulation of a Real Lime Kiln Plant to Understand Ring Formation Phenomena. *Processes* **2025**, *13*, 1022. https://doi.org/10.3390/pr13041022

1. Introduction

This paper presents a modeling study aimed at enhancing the understanding of ring formation in lime kilns through simulation. This study was developed based on data from a plant owned by The Navigator Company, located in Setúbal, Portugal. The research focuses on the chemical recovery cycle integrated into the pulp production process at a pulp mill, with particular emphasis on the calcium cycle involving two parallel lime kilns operating continuously. These kilns are critical to the process, and their unavailability can significantly affect the overall cost-effectiveness of the facility [1].

The calcination of lime sludge takes place in a rotary kiln, where combustion energy and lime sludge circulate in a countercurrent flow. This process converts the calcium carbonate in the lime sludge into calcium oxide (lime), releasing carbon dioxide in the

process. Under certain conditions, material progressively accumulates at specific points in the kiln, leading to the gradual formation of rings. If unchecked, this buildup can eventually clog the kiln, requiring intervention and resulting in operational downtime. This is one of the main causes of the equipment's unavailability.

Several types of rings can form in lime kilns, but it is widely agreed that the most problematic are those that develop in the middle zone of the furnace, equidistant from both ends [2].

The causes of ring formation have been extensively studied by various research groups from the late 1980s to the present [3–5]. However, it is not possible to identify a single cause for ring formation. The variety of ring geometries and the different operating modes of these processes contribute to the diversity of explanations. This implies that studying these phenomena at a specific plant requires considering the unique characteristics of that plant.

The sticking of the particles to the kiln walls is partially attributed to the fusion of sodium carbonate Na_2CO_3 and sodium sulphate Na_2SO_4 present in the sludge.

Once the sludge adheres to the kiln walls, hardening is primarily caused by recarbonation. In this process, CaO (calcium oxide or lime) is converted back into $CaCO_3$ (calcium carbonate), which strengthens the ring structure. Recarbonation is favored by low temperatures and high CO_2 concentrations [6,7]. In kilns that burn fuels with high sulfur content, the hardening of existing rings can also be caused by sulfation.

Sodium tends to accumulate inside lime kilns due to an internal cycle in which sodium vaporizes in the high-temperature zone and is subsequently transported to the sludge feed zone, where it condenses again [8]. Sodium also tends to concentrate in the dust fraction, as evidenced by the fact that the sodium content in lime sludge dust is approximately two to three times higher than in the feed sludge [7].

The link between non-stationary operation and ring formation is established through fluctuations in the temperature profile along the length of the kiln, particularly in the calcination zone, which promotes the recarbonation of lime. An analysis of three furnaces reported in the literature [9] showed that the temperature profile is closely tied to furnace operation and the potential formation of rings. Moreover, temperature fluctuations within the kiln significantly contribute to this issue. The results of this study confirm that minimizing process variability can be an effective strategy to reduce the frequency of ring formation in lime kilns.

Burning a single, high-quality fuel with stable parameters is naturally easier to control. However, the need to burn strong gases extracted from other production areas—resulting in energy recovery and a positive environmental impact—introduces variability into the process operation [10,11].

Process operation and control are also sources of variability [12]. Manually operating a lime kiln is challenging, and automating its control is a complex task. The calcination dynamics are complicated by nonlinear chemical kinetics, long delay times, and variable feed characteristics [13].

Another factor linked to ring formation due to process variability is the appearance and behavior of the flame inside the furnace and its impact on the temperature profile [14,15]. An unstable flame causes significant variations in gas temperatures, which can lead to the recarbonation of lime, as previously mentioned [16].

The combustion of non-condensable gases (NCG)—including strong gases and gases from the stripper—as fuel has been identified by several sources [14,16–19] as a contributing factor to ring formation due to their high sulfur content. Sulfur not only promotes ring formation but also contributes to their hardening, making natural removal more difficult.

Regarding the modeling of lime kilns and ring formation, the authors of [20] developed both static and dynamic models for the calcination process and lime kilns. However, the

level of detail provided in their work is insufficient. The model appears to be empirical, resembling a black-box approach. Moreover, the industrial data used to validate the models or assess their applicability are not available. According to the authors, the dynamic models were successfully implemented in a new control system for the causticizing and lime kiln process [21].

Furthermore, the authors of [22] present simulation results of a lime kiln process based on a one-dimensional CFD model, but no details are provided about the model's development. More recently, some studies have developed higher dimensional models (2D gas and 1D model) [23] for steady-state analysis. Reference [24] recently conducted a survey study on the modeling, control, and instrumentation of lime kiln processes, describing the process as a lumped system.

Therefore, the authors developed a physics-based model to simulate the internal behavior of the kiln using real plant data, including lime sludge and fuel flows, among other inputs. Significant partial support for this development was obtained from references [25,26].

This paper describes all the chemical reactions and thermodynamic processes involved. The developed model follows a finite-dimensional approach and is one-dimensional, modeling only the longitudinal variation. Several judicious approximations were made to keep the simulation time within a reasonable limit. The adoption of a one-dimensional approach was a deliberate choice to strike a balance between model complexity and computational efficiency. A fully three-dimensional model would require significantly more computational resources and detailed input data, which were not available from the plant instrumentation. Moreover, the primary objective of this study was to capture the key longitudinal dynamics of the calcination process and ring formation, which are predominantly influenced by variations along the kiln's length. While radial and cross-sectional variations can provide additional insights, the longitudinal profile remains the dominant factor in the overall process behavior.

The main result of this work is the consolidation of all necessary information to develop a comprehensive kiln model, addressing the gaps in existing literature, which often lacks the detailed data and insights required for accurately modeling lime kiln dynamics.

2. Process Description

This study focuses on the chemical recovery cycle integrated into the pulp production process (Figure 1), with particular emphasis on the calcium cycle involving two lime kilns in continuous operation. These kilns are critical to the process, and their unavailability can significantly impact on the overall profitability of the facility [27].

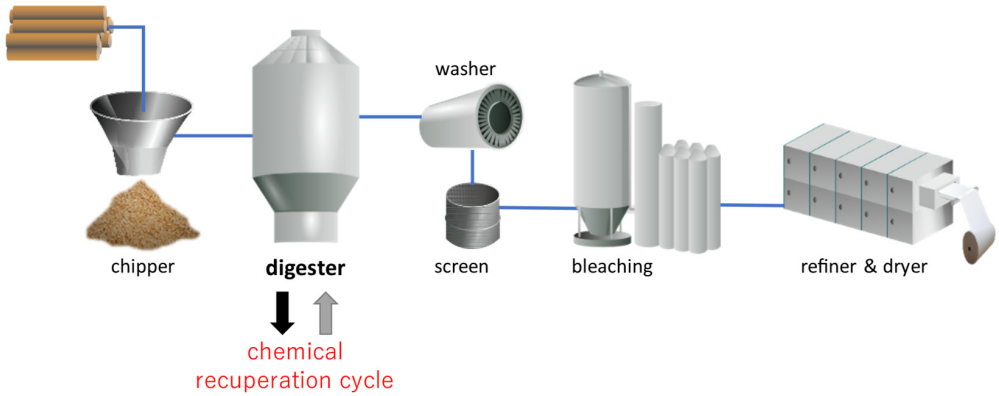

Figure 1. Position of the chemical recovery cycle in the pulp production process.

The chemical recovery cycle is linked with the cooking of wood chips in the kraft process. In the kraft process, wood is transformed into pulp through a chemical reaction involving the so-called white liquor, which consists of sodium hydroxide (NaOH) and sodium sulfide (Na_2S). This process produces raw pulp and black liquor. Black liquor, which results from the dissolution of lignin during digestion, is primarily composed of sodium sulfate (Na_2SO_4) and sodium carbonate (Na_2CO_3).

The chemical recovery cycle regenerates white liquor from black liquor, preventing the environmental issue of effluent disposal and reducing the need to purchase fresh reagents for the process. It also enables energy recovery from the combustion of dissolved lignin, which is used for electrical energy production.

The recovery process consists of two integrated cycles: the sodium cycle and the calcium cycle, as shown in the diagram in Figure 2.

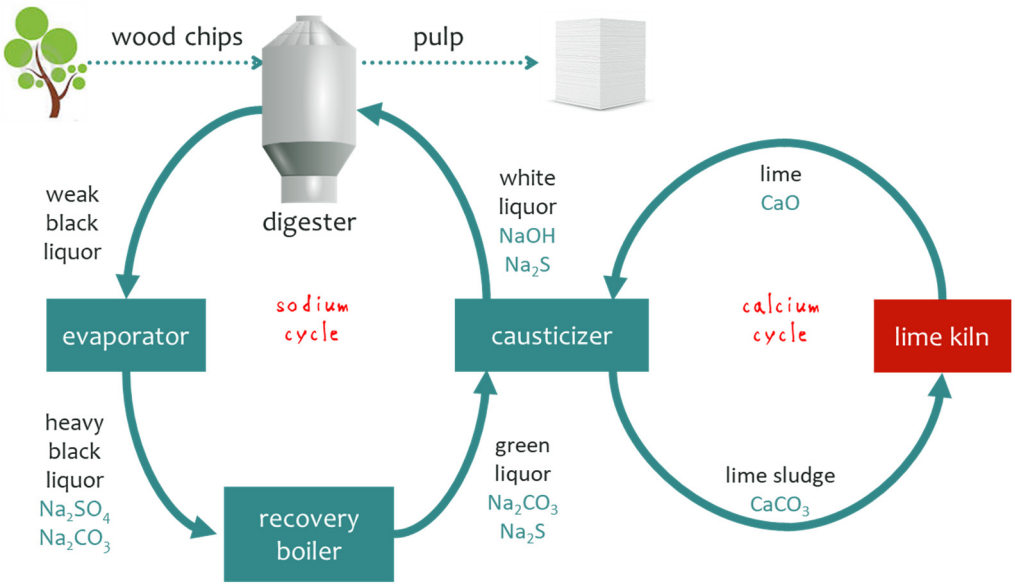

Figure 2. Sodium and calcium cycles in the chemical recovery process.

The weak black liquor, produced from cooking and washing, undergoes an evaporation process to remove water, resulting in strong black liquor. This by-product is fed into the recovery boiler, where energy recovery takes place, producing a solution of sodium salts known as green liquor. In the next step, during the causticizing process, sodium carbonate is converted into sodium hydroxide, completing the sodium cycle and producing white liquor, which is ready for cooking new wood chips.

In the causticizing step, which requires fresh lime, lime mud is produced as a by-product. The calcium cycle regenerates fresh lime from the lime mud.

The calcium cycle consists of three key steps relevant to the problem under study:

- Washing lime mud;
- Thickening lime mud;
- Calcination in the lime kiln.

Washing the lime mud is essential for reducing sodium content, which helps lower subsequent sulfite emissions. Thickening reduces the water content before calcination in the kilns.

Ring Formation Phenomenon in Lime Kilns

The calcination process takes place in a rotary kiln (Figure 3), where combustion energy and lime mud circulate in a countercurrent flow. This process transforms the

calcium carbonate present in the lime mud into calcium oxide (lime), releasing carbon dioxide as a by-product.

Figure 3. Picture of the rotary lime kiln object of this study (courtesy of The Navigator Company).

The calcination reaction is represented by the following chemical equation:

$$CaCO_3(s) + \text{heat} \rightarrow CaO(s) + CO_2(g) \quad (1)$$

where $CaCO_3$ is calcium carbonate, CaO is calcium oxide and CO_2 is carbon dioxide, released in gaseous form.

The mud progressively passes through the drying, heating, and calcination zones before the lime is discharged in the cooling satellites, as depicted in Figure 4.

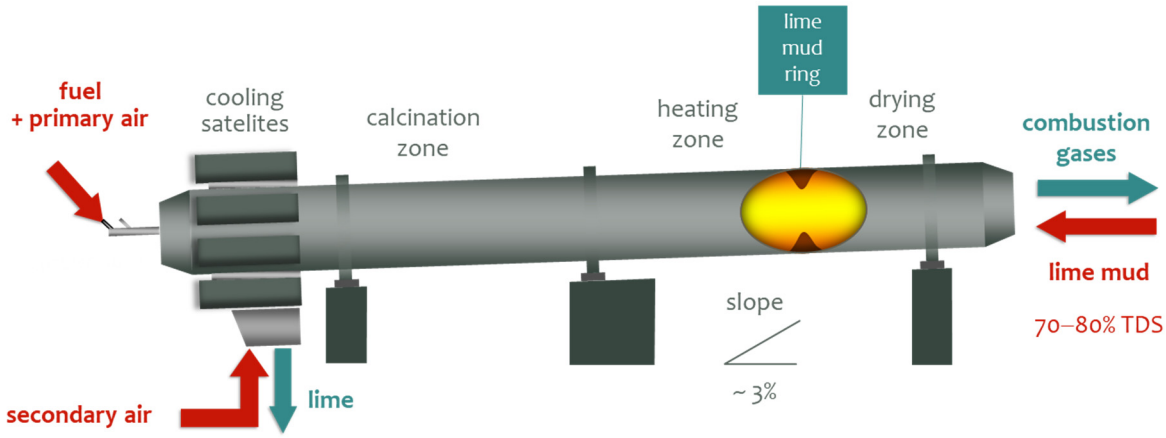

Figure 4. Schematic of the calcination process in the lime kiln.

The operability of the calcination process and the quality of the final product depend on several factors, including the moisture content of the sludge, its sodium content, the temperature distribution in the furnace, and the oxygen content during combustion.

Under certain conditions, material progressively accumulates at specific points in the furnace, leading to the gradual formation of rings. If unchecked, this buildup can eventually clog the furnace, requiring intervention and causing operational downtime. This is one of the primary causes of equipment unavailability.

The location of ring formation within the kiln provides insight into the physicochemical phenomenon responsible for its formation, and extensive knowledge about this problem already exists in the literature.

The question of ring formation is not if it will happen—it is inevitable—but rather when the next occurrence will be. However, the exact operating conditions that promote ring formation are not yet fully understood, which highlights the importance of this study.

3. Lime Kiln Modelling Process

This section describes the dynamic modeling process based on the spatial distribution characteristics of the installation. The modeling process is inherently an approximation exercise, and any model has its specific operating range and limits of validity.

A well-executed modeling process should strike the best balance between computational effort and the relevance of the results. In this specific modeling process, the following approximations were made:

- The variation in the spatial domain, for both the bed and the gases, was considered only in one dimension. In other words, only variations along the longitudinal axis of the kiln are modeled. The two-dimensional distribution of physical variables across different cross-sections of the furnace is not considered. The complexity of three-dimensional modeling (in the domain of CFD) exceeds the scope of this study and the availability of data from plant instrumentation.
- All gases were aggregated into a single gaseous mass. The main implication of this approximation is the averaging of the specific heat and molar mass values of individual constituent gases. However, this simplification does not affect the dynamics of mass, energy, or momentum conservation. Aggregating all gases into a single mass is a reasonable approximation because the primary focus of the model is on capturing the longitudinal variations along the kiln rather than the detailed local gas–solid interactions. In lime kilns, the overall mass and energy balance are often dominated by the bulk flow and heat transfer dynamics rather than species-specific variations. Moreover, since the major gas components (CO_2 and H_2O) have similar thermal properties within the typical operating range, treating them as a single mass introduces minimal error in the overall energy and mass balance calculations.
- The specific heat values of the various species were assumed to be constant, i.e., independent of temperature. This simplification, which has a minimal impact on the species under consideration, was adopted to accelerate the simulation.
- The latent heat of evaporation and the enthalpy of the calcination reaction were also assumed to be constant to accelerate numerical integration during the simulation.
- The linear velocity of the bed was assumed to be independent of the longitudinal position, meaning that while the velocity varies over time, it remains uniform throughout the entire furnace. It should be noted that since the mass changes during the drying and calcination processes, the mass flow rate depends on the process zone, even when the velocity is constant over time.

The appropriate way to develop a dynamic model of a distributed process is to simultaneously account for both time and space. This requires the process simulation to numerically integrate these two variables, which appear in the mathematical model as equations involving multiple partial derivatives.

The classic approach to solving this problem is to divide the spatial domain into a grid of finite elements. In this study, since spatial variation is considered only in one dimension, the kiln is discretized into N finite elements, representing N sections of the kiln, each with a length of Δx. Figure 5 provides a supporting diagram for the model, showing the main variables considered, which include the following:

- x—longitudinal position, increasing in the direction of the gas flow;
- t—time variable;
- $T_b(x,t)$—bed temperature, as a function of time and space;
- $T_g(x,t)$—gas temperature, as a function of time and space;
- $T_b^i(t)$—bed temperature at element i, as a function of time, i.e., $T_b^i(t) = T_b(x_i,t)$;
- $T_g^i(t)$—gas temperature at element i, as a function of time, i.e., $T_g^i(t) = T_g(x_i,t)$;
- $v_b(t)$—bed velocity, as a function of time;
- $v_g(x,t)$—gas velocity, as a function of time and space.

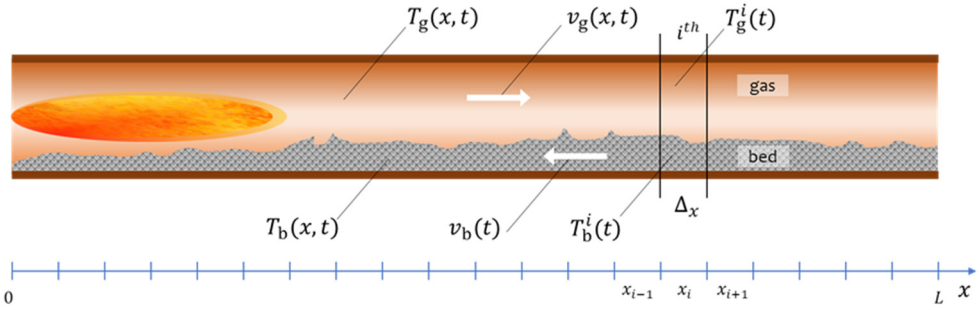

Figure 5. Schematic of the calcination process in the lime kiln with the main modelling variables.

The dynamic model is based on the mass and energy conservation equations (also known as continuity equations) for both the bed and the gases.

3.1. Bed Equations

The first set of equations is developed for the bed, considering the lime sludge feed. The sludge consists of water, which evaporates along the length of the kiln, increasing the gas flow, and calcium carbonate ($CaCO_3$), which is converted into calcium oxide (CaO) during the calcination process.

3.1.1. Bed Continuity Equations—One Dimensional

The following equations represent the conservation of mass and energy in the bed, respectively:

$$\frac{\partial A\rho_b(x,t)}{\partial t} - v_b(t)\frac{\partial A\rho_b(x,t)}{\partial x} = M_{bs}(x,t) \tag{2}$$

$$\frac{\partial Ah_b(x,t)\rho_b(x,t)}{\partial t} - v_b(t)\frac{\partial Ah_b(x,t)\rho_b(x,t)}{\partial x} = Q_{bs}(x,t) \tag{3}$$

where

- $\rho_b(x,t)$—bed density [kg/m^3];
- $h_b(x,t)$—bed specific enthalpy [J/kg];
- $v_b(t)$—bed velocity [m/s] (opposite to the positive direction of the x-axis);
- A—transversal area [m^2];
- $M_{bs}(x,t)$—source/drain mass balance [kg/s/m];
- $Q_{bs}(x,t)$—source/drain energy balance [W/m].

The left side of each equation represents the transport effect of the moving fluid's properties over time and space, while the right side accounts for the gains (if positive) or losses (if negative) from mass and energy exchange with the surroundings. Here, the surroundings include the gases in contact with the bed (for mass and energy exchange) and the kiln walls (for energy exchange).

When simulating the system, it is also necessary to define the boundary conditions for the mass and energy inputs at the ends of the kiln, at $x = 0$ and $x = L$, where L is the length of the rotary kiln.

It should be noted that the density represented by the variable ρ_b, like the densities that will appear later in the model, does not correspond to the specific density of the material. For modeling purposes, the total volume of each finite element is given by $A \cdot \Delta_x$.

The mass flow, in kg/s, is related to the previous variables as follows:

$$q_b(x,t) = A \cdot \rho_b(x,t) \cdot v_b(t) \tag{4}$$

and this variable has a straightforward interpretation consistent with its conventional meaning.

In the bed, the lime sludge undergoes a drying process (evaporation of water) and a calcination process, which converts calcium carbonate into calcium oxide, governed by the following chemical reaction:

$$\mathrm{CaCO_3} \rightarrow \mathrm{CaO} + \mathrm{CO_2(g)} \tag{5}$$

with the corresponding release of carbon dioxide (CO_2) and retention of energy. Therefore, four species are involved in bed modeling: $CaCO_3$, CaO, CO_2 and H_2O. The mass conservation equation can be written as follows:

$$\frac{\partial A\rho_k}{\partial t} - v_\mathrm{b}\frac{\partial A\rho_k}{\partial x} = M_k \tag{6}$$

where the variable k indicates the species involved. Since carbon dioxide is released immediately in gaseous form, there is no need to apply a mass conservation equation on the solid side.

The calcination and evaporation processes were modeled using the Arrhenius equation [25,26], which describes the reaction rates as a function of the bed temperature. Thus, the rates of mass variation for each species are given by the following equations:

$$k = \mathrm{CaCO_3} \qquad M_\mathrm{CaCO3} = -\rho_\mathrm{CaCO3} \cdot A \cdot A_\mathrm{calc} \mathrm{e}^{-\frac{E_\mathrm{calc}}{R \cdot T_\mathrm{b}}} \tag{7}$$

$$k = \mathrm{CaO} \qquad M_\mathrm{CaO} = -\frac{MM_\mathrm{CaO}}{MM_\mathrm{CaCO3}} \cdot M_\mathrm{CaCO3} \tag{8}$$

$$k = \mathrm{H_2O} \qquad M_\mathrm{H2O} = -\rho_\mathrm{H2O} \cdot A \cdot A_\mathrm{evap} \mathrm{e}^{-\frac{E_\mathrm{evap}}{R \cdot T_\mathrm{b}}} \tag{9}$$

$$k = \mathrm{CO_2} \qquad M_\mathrm{CO2} = -\frac{MM_\mathrm{CO2}}{MM_\mathrm{CaCO3}} \cdot M_\mathrm{CaCO3} \tag{10}$$

where

- MM_CaO, MM_CO2 and MM_CaCO3 are molar masses;
- A_calc and A_evap are the pre-exponential factors for the calcination and evaporation reactions;
- E_calc and E_evap are the energetic activation factors for calcination and vaporization reactions;
- R is the universal constant of perfect gases in J/mol/K.

Regarding energy conservation, the balance of energy sources/sinks is given by the following equation:

$$Q_\mathrm{bs} = Q_\mathrm{gb} - Q_\mathrm{calc} - Q_\mathrm{evap} - Q_\mathrm{bw} \tag{11}$$

where Q_{gb} is the energy transferred from the gases to the bed; Q_{calc} and Q_{evap} are the energy values consumed by the calcination and evaporation reactions, respectively, and are defined as follows:

$$Q_{calc} = -H_{calc} \cdot M_{CaCO3} \tag{12}$$

$$Q_{evap} = -H_{evap} \cdot M_{H2O} \tag{13}$$

where H_{calc} and H_{evap} are the enthalpy of the calcination reaction and the latent heat of water evaporation, respectively, in J/kg.

The total density of the bed (since all densities are relative to the total volume of the element) is given by

$$\rho_b = \rho_{CaCO3} + \rho_{CaO} + \rho_{H2O} \tag{14}$$

3.1.2. Bed Continuity Equations—Discretization

As previously mentioned, preparing the model equations for numerical integration requires spatial discretization. Thus, the mass conservation equation for each species k is as follows:

$$\frac{\partial A\rho_k}{\partial t} - v_b \frac{\partial A\rho_k}{\partial x} = M_k \tag{15}$$

Since the cross-sectional area A is assumed to be constant, the discrete-space version of the ordinary differential equation (ODE) becomes the following:

$$\frac{d\rho_k^i}{dt} - v_b \frac{\rho_k^{i+1} - \rho_k^i}{\Delta x} = \frac{1}{A} M_k$$

or

$$\frac{d\rho_k^i}{dt} = \frac{v_b}{\Delta x}\rho_k^{i+1} - \frac{v_b}{\Delta x}\rho_k^i + \frac{1}{A} M_k \tag{16}$$

Similarly, the energy conservation equation is as follows:

$$\frac{\partial h_b \rho_b}{\partial t} - v_b \frac{\partial h_b \rho_b}{\partial x} = \frac{1}{A} Q_{bs} \tag{17}$$

which results in the discrete-space version of the ODE shown below:

$$\frac{dh_b^i \rho_b^i}{dt} - v_b \frac{h_b^{i+1}\rho_b^{i+1} - h_b^i \rho_b^i}{\Delta x} = \frac{1}{A} Q_{bs}$$

or

$$\rho_b^i \frac{dh_b^i}{dt} = -h_b^i \frac{d\rho_b^i}{dt} + \frac{v_b}{\Delta x} h_b^{i+1}\rho_b^{i+1} - \frac{v_b}{\Delta x} h_b^i \rho_b^i + \frac{1}{A} Q_{bs}$$

and finally,

$$\frac{dh_b^i}{dt} = \frac{1}{\rho_b^i}\left\{ -h_b^i \frac{d\rho_b^i}{dt} + \frac{v_b}{\Delta x} h_b^{i+1}\rho_b^{i+1} - \frac{v_b}{\Delta x} h_b^i \rho_b^i + \frac{1}{A} Q_{bs} \right\} \tag{18}$$

3.2. Gas Equations

As previously mentioned, the dynamic modeling of a spatially distributed system is performed using partial differential equations.

3.2.1. Gas Continuity Equations—One Dimensional

The equations for mass and energy continuity are, at their core, identical to those used for the bed solids, as shown below:

$$\frac{\partial A\rho_g(x,t)}{\partial t} + v_g(x,t) \frac{\partial A\rho_g(x,t)}{\partial x} = M_{gs}(x,t) \tag{19}$$

$$\frac{\partial A h_g(x,t)\rho_g(x,t)}{\partial t} + v_g(x,t)\frac{\partial A h_g(x,t)\rho_g(x,t)}{\partial x} = Q_{gs}(x,t) \quad (20)$$

where

- $\rho_g(x,t)$—is the gas density [kg/m^3];
- $h_g(x,t)$—gas specific enthalpy [J/kg];
- $v_g(x,t)$—gas velocity [m/s] (concurrent to the positive direction on the x-axis);
- $M_{gs}(x,t)$—source/drain mass balance [kg/s/m];
- $Q_{gs}(x,t)$—source/drain energy balance [W/m],

The sources of mass are related to the evaporated water, represented by $(-M_{H2O})$ and the carbon dioxide resulting from calcination, given by M_{CO2}, which are both positive. Therefore,

$$M_{gs} = M_{CO2} + (-M_{H2O}) \quad (21)$$

The energy sources and sinks are related to the following:

- Q_{CH4}—heat input from the combustion of fuel;
- Q_{gb}—gas-bed heat transfer;
- Q_{gw}—heat losses to the kiln wall.

The total energy balance is given by

$$Q_{gs} = Q_{CH4} - Q_{gb} - Q_{gw} \quad (22)$$

Next, we introduce the gas expansion effect. The equation of state for an ideal gas is as follows:

$$P \cdot V = n \cdot R \cdot T_g \quad (23)$$

where

- P—pressure [N/m^2];
- V—volume [m^3];
- n—number of moles [mol];
- T—gas temperature [K].

By definition,

$$n = \frac{\rho_g \cdot V}{MM_g} \quad (24)$$

where MM_g is the molar mass of the gas in [kg/mol]. Substituting this into Equation (23), we obtain

$$\rho_g = \frac{P \cdot MM_g}{R \cdot T_g} \quad (25)$$

Assuming constant pressure and taking the time derivative of Equation (25) gives the following equation:

$$\frac{d\rho_g}{dt} = \frac{P}{R \cdot T}\frac{dMM_g}{dt} - \frac{P \cdot MM_g}{R \cdot T_g^2}\frac{dT_g}{dt} \quad (26)$$

This equation, together with Equations (19) and (20), allows us to determine not only the enthalpy and density profiles but also the spatial profile of the gas velocity, $v_g(x,t)$.

3.2.2. Gas Continuity Equations—Discretization

The equations related to the gases are also discretized in space to enable numerical integration, resulting in

$$\frac{\partial A\rho_g}{\partial t} + v_g\frac{\partial A\rho_g}{\partial x} = M_{gs} \quad (27)$$

for the mass conservation. Assuming a constant cross-sectional area A, the equation becomes

$$\frac{d\rho_{\mathrm{g}}^{i}}{dt}+\frac{v_{\mathrm{g}}^{i}\rho_{\mathrm{g}}^{i}-v_{\mathrm{g}}^{i-1}\rho_{\mathrm{g}}^{i-1}}{\Delta x}=\frac{1}{A}M_{\mathrm{gs}} \tag{28}$$

which will be used to calculate the velocity in element i as follows:

$$v_{\mathrm{g}}^{i}=\frac{1}{\rho_{\mathrm{g}}^{i}}\left(v_{\mathrm{g}}^{i-1}\rho_{\mathrm{g}}^{i-1}-\Delta x\frac{d\rho_{\mathrm{g}}^{i}}{dt}+\frac{\Delta x}{A}M_{\mathrm{gs}}\right) \tag{29}$$

From Equation (26), assuming an approximately constant molar mass of the gases, we obtain

$$\frac{d\rho_{\mathrm{g}}^{i}}{dt}=-\frac{P\cdot MM_{\mathrm{g}}}{R\cdot\left(T_{g}^{i}\right)^{2}}\frac{dT_{\mathrm{g}}^{i}}{dt}=-\frac{P\cdot MM_{\mathrm{g}}}{c_{\mathrm{pg}}\cdot R\cdot\left(T_{g}^{i}\right)^{2}}\frac{dh_{\mathrm{g}}^{i}}{dt} \tag{30}$$

which shows the direct relationship between the gas density and its energy content, as expected.

Regarding energy conservation of energy, we obtain

$$\frac{\partial Ah_{\mathrm{g}}\rho_{\mathrm{g}}}{\partial t}+v_{\mathrm{g}}\frac{\partial Ah_{\mathrm{g}}\rho_{\mathrm{g}}}{\partial x}=Q_{\mathrm{gs}} \tag{31}$$

Assuming a constant cross-sectional area A, this results in the following equation:

$$\frac{dh_{\mathrm{g}}^{i}\rho_{\mathrm{g}}^{i}}{dt}+\frac{v_{\mathrm{g}}^{i}h_{\mathrm{g}}^{i}\rho_{\mathrm{g}}^{i}-v_{\mathrm{g}}^{i-1}h_{\mathrm{g}}^{i-1}\rho_{\mathrm{g}}^{i-1}}{\Delta x}=\frac{1}{A}Q_{\mathrm{gs}} \tag{32}$$

or

$$\rho_{\mathrm{g}}^{i}\frac{dh_{\mathrm{g}}^{i}}{dt}+h_{\mathrm{g}}^{i}\frac{d\rho_{\mathrm{g}}^{i}}{dt}=\frac{v_{\mathrm{g}}^{i-1}h_{\mathrm{g}}^{i-1}\rho_{\mathrm{g}}^{i-1}}{\Delta x}-\frac{v_{\mathrm{g}}^{i}h_{\mathrm{g}}^{i}\rho_{\mathrm{g}}^{i}}{\Delta x}+\frac{1}{A}Q_{\mathrm{gs}} \tag{33}$$

resulting in the following equation:

$$\frac{dh_{\mathrm{g}}^{i}}{dt}=\frac{1}{\rho_{\mathrm{g}}^{i}}\left(-h_{\mathrm{g}}^{i}\frac{d\rho_{\mathrm{g}}^{i}}{dt}+\frac{v_{\mathrm{g}}^{i-1}h_{\mathrm{g}}^{i-1}\rho_{\mathrm{g}}^{i-1}}{\Delta x}-\frac{v_{\mathrm{g}}^{i}h_{\mathrm{g}}^{i}\rho_{\mathrm{g}}^{i}}{\Delta x}+\frac{1}{A}Q_{\mathrm{gs}}\right) \tag{34}$$

Using Equation (29) in Equation (34), after some manipulation, we obtain

$$\frac{dh_{\mathrm{g}}^{i}}{dt}=\frac{1}{\rho_{\mathrm{g}}^{i}}\left(v_{\mathrm{g}}^{i-1}\rho_{\mathrm{g}}^{i-1}+\frac{h_{\mathrm{g}}^{i-1}-h_{\mathrm{g}}^{i}}{\Delta x}-\frac{h_{\mathrm{g}}^{i}}{\mathrm{A}}M_{\mathrm{gs}}+\frac{1}{A}Q_{\mathrm{gs}}\right) \tag{35}$$

The temperature is derived from the specific enthalpy using the relationship as follows:

$$dh_{g}=c_{\mathrm{pg}}\cdot dT_{g} \tag{36}$$

Tables 1–3 present the list of the main variables, the list of parameters for the specific unit and the list of constants used in the model, respectively.

The model described above was implemented in Simulink, part of the MATLAB package (MathWorks, version 2016b). The number of elements was chosen based on the process time constant and the length of each section, and was rounded up to n = 100 elements, as shown in Figure 6. Figure 7 provides a more detailed view of the model's structure, illustrating the internal blocks within each element.

Table 1. List of main variables used in the model.

Description of the Variable	Symbol	Unit
Bed density	$\rho_{\mathrm{b}}(x,t)$	$\mathrm{kg/m^3}$
Density of species k	$\rho_k(x,t)$	$\mathrm{kg/m^3}$
Gas density	$\rho_{\mathrm{g}}(x,t)$	$\mathrm{kg/m^3}$
Enthalpy of solids in the bed	$h_b(x,t)$	J/kg
Enthalpy of gases	$h_{\mathrm{g}}(x,t)$	J/kg
Mass source	$M_{\mathrm{s}}(x,t)$	kg/s/m
Mass source of species k	$M_k(x,t)$	kg/s/m
Power supply	$Q_{\mathrm{s}}(x,t)$	W/m
Bed temperature	$T_{\mathrm{b}}(x,t)$	K
Gas temperature	$T_{\mathrm{g}}(x,t)$	K
Bed velocity	$v_{\mathrm{b}}(t)$	m/s
Gas velocity	$v_{\mathrm{g}}(x,t)$	m/s

Table 2. List of parameters used in the model (unique for the specific kiln unit).

Parameter	Symbol	Value	Unit
Cross-sectional area	A	7.06	$\mathrm{m^2}$
Bed-specific heat	c_{b}	1.088×10^3	J/kg/K
Internal diameter	D	3.0	m
Kiln length	L	90.0	m
Number of sections	n	100	–
Ambient temperature	T_0	298.15	K
Section length	Δx	0.90	m
Flame length	x_{f}	20.0	m

Table 3. List of constants used in the model (independent of the specific kiln unit).

Symbol in the Model	Value	Unit
A_{calc}	1.0×10^8	$\mathrm{s^{-1}}$
A_{evap}	2.55×10^7	$\mathrm{s^{-1}}$
c_{b}	1.088×10^3	J/kg/K
c_{pg}	1.550×10^3	J/kg/K
E_{calc}	220.728×10^3	J/mol
E_{evap}	40.664×10^3	J/mol
H_{calc}	1.9850×10^6	J/kg
H_{evap}	2.2572×10^6	J/kg
H_{CH4}	55.21×10^6	J/kg
MM_{CaO}	56.07×10^{-3}	kg/mol
MM_{CO2}	44.01×10^{-3}	kg/mol
MM_{CaCO3}	100.08×10^{-3}	kg/mol
MM_{CH4}	16.04×10^{-3}	kg/mol
MM_{H2O}	18.02×10^{-3}	kg/mol
MM_{O2}	32.00×10^{-3}	kg/mol
MM_{g}	27.70×10^{-3}	kg/mol
P_0	101,325.0	$\mathrm{N/m^2}$
R	8.3145	J/mol/K
T_0	298.0	K

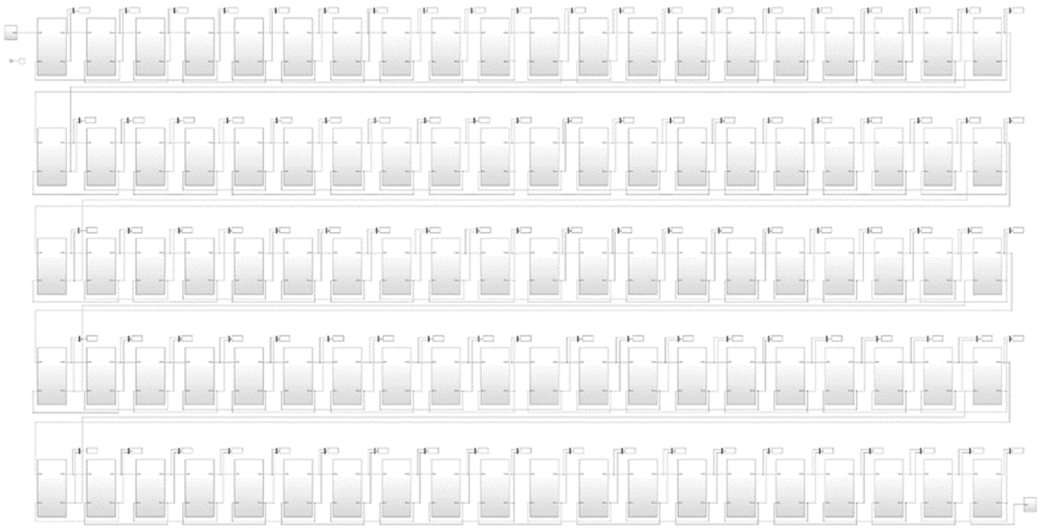

Figure 6. Realization in SimuLink-MATLAB of the model with $n = 100$ elements.

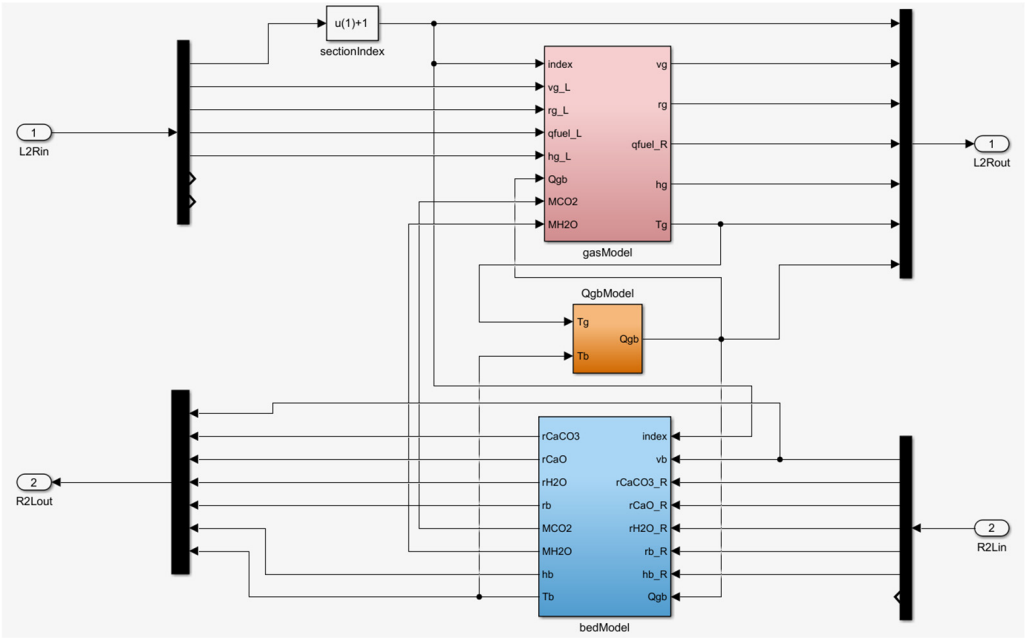

Figure 7. Realization in SimuLink-MATLAB of the model in each element.

4. Results and Discussion

With the implementation of the model in the simulation environment, the authors developed a set of simulations to explore its use towards a better understanding of the dynamic behavior of the plant.

4.1. Steady-State Simulation Results

The initial simulations were conducted with constant inputs, i.e., stationary boundary conditions, over periods equivalent to ten hours of kiln operation. The objective was to establish a steady-state equilibrium profile to be used as the initial state for subsequent simulations. Figures 8–11 show the steady-state profiles for temperatures, gas-bed heat transfer, bed mass flows, and gas velocity and density.

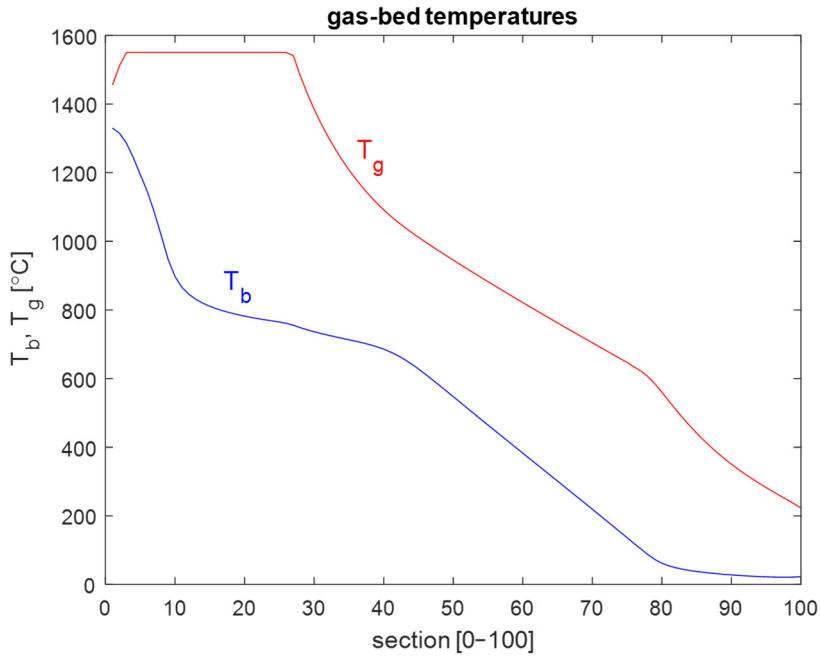

Figure 8. Steady-state temperature profile (after 10 h).

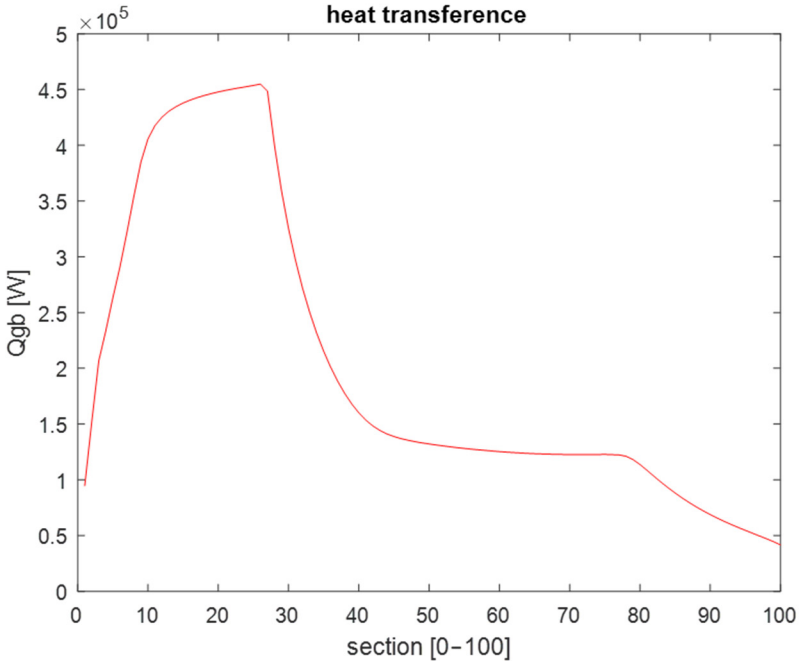

Figure 9. Steady-state gas-bed heat transfer (after 10 h).

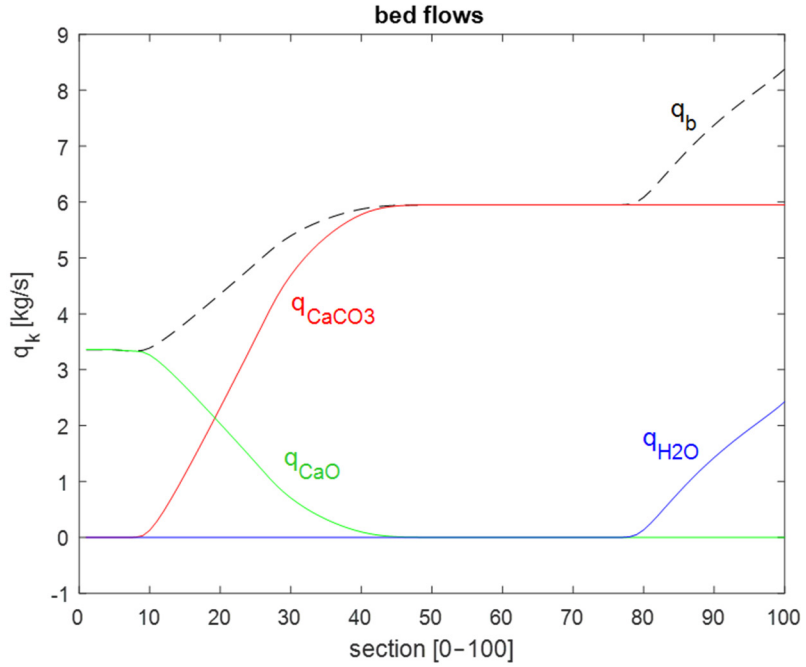

Figure 10. Steady-state mass flows (after 10 h).

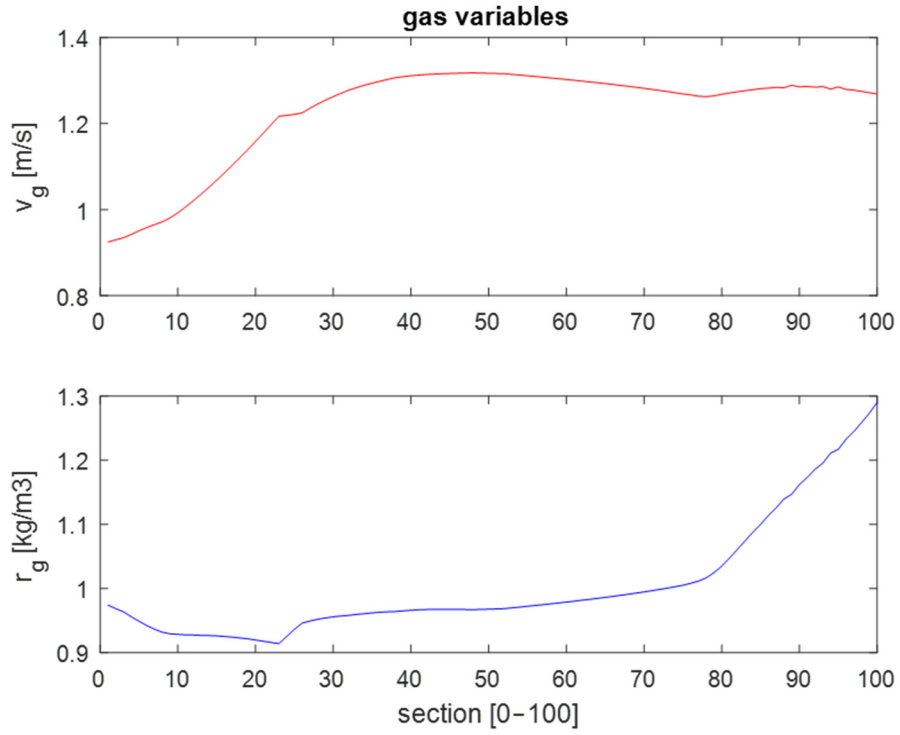

Figure 11. Steady-state gas velocity and density (after 10 h).

4.2. Simulation Results with Real Plant Data

After developing and calibrating the model—including the parameterization of initial conditions and boundary values—simulation tests were conducted to identify conditions conducive to ring formation, which is the overall objective of this work.

The test presented below is representative of the model's analytical potential.

One of the primary causes of mid-kiln ring formation is variability in kiln operation, particularly fluctuations in fuel flow rates (including NCG).

For this representative test, real plant data were used over a 10 h period. During this period, the sludge flow rate and rotation speed were kept constant at steady values of

11 l/s, and 1.4 rpm, respectively. Figure 12 shows the sum of fuel and NCG flow rates during this period, with the NCG containing approximately 80% methanol. This signal, referred to as q_{fuel} and directly linked to the model variable Q_{CH4}, was used as a boundary condition in the simulation test.

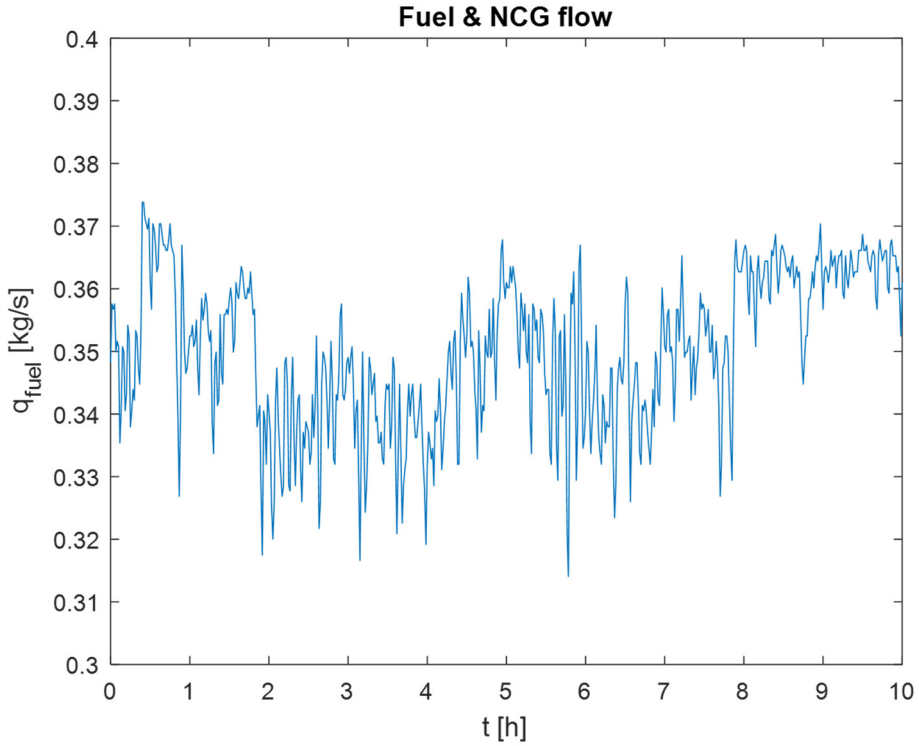

Figure 12. Real input data for fuel flow (including NCG)—10 h period.

Figures 13 and 14 illustrate the impact of energy flow fluctuations on the stationarity of the temperature profiles of both the solid bed and the gases.

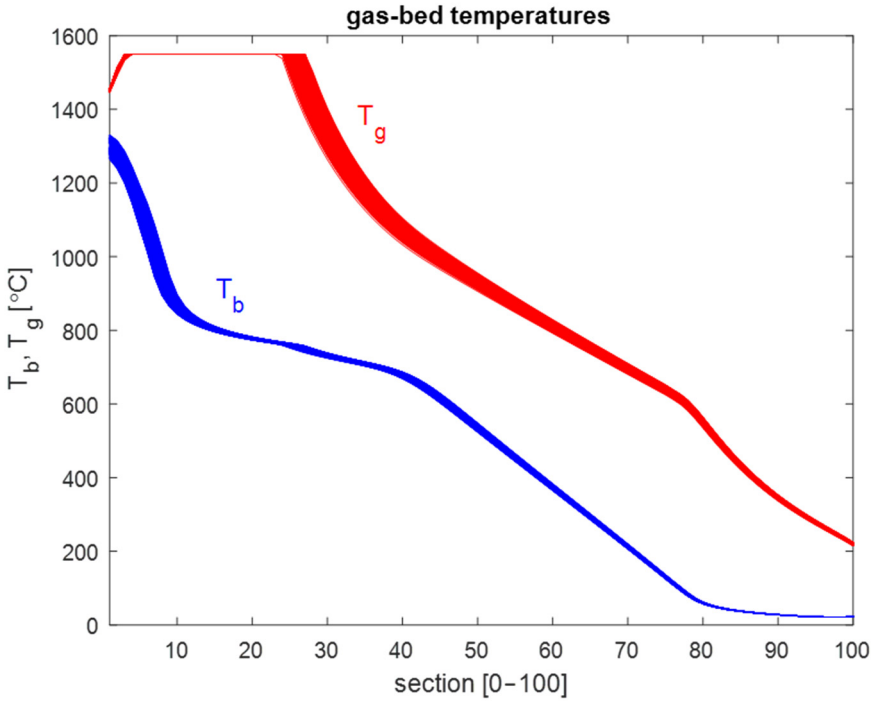

Figure 13. Superposition of bed and gas temperature profiles over a 10 h period.

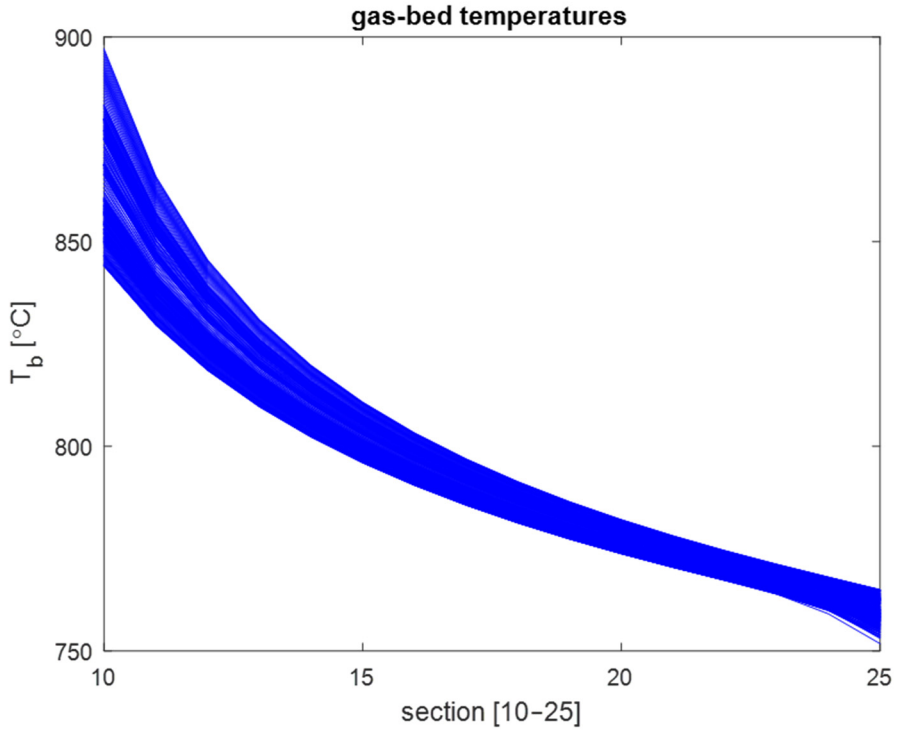

Figure 14. Details of the bed temperature profiles across the calcination temperature.

Note that the estimated linear velocity of the sludge used in the simulation is 0.01 m/s, which corresponds to a residence time of 9000 s (or 2.5 h). In other words, the residence time of the calcium pathway inside the kiln is on the same order of magnitude as the 10 h simulation period.

4.3. Discussion of the Observed Simulation Results

According to several studies on the subject, one of the causes of ring formation is variability in kiln operation, particularly fluctuations in fuel flow rates and the presence of sulfur from the addition of NCG to the fuel for incineration. Simulations based on real operational data confirmed fluctuations in energy flows, which affected the stability of the temperature profiles of both the solid and gas beds. These fluctuations are particularly critical in the calcination zone, where the thermal balance is delicate, and even minor deviations can lead to uneven heating and cooling of the lime sludge.

The simulation tests presented above indicate that masses of lime sludge experience periods of cooling before reaching the outlet for the coolers, which promotes the recarbonation of lime and, consequently, the formation of rings. Recarbonation occurs when calcium oxide (CaO) reacts with carbon dioxide (CO_2) to form calcium carbonate ($CaCO_3$), which hardens and adheres to the kiln walls. Similar adhesion and hardening phenomena due to recarbonation have been observed in other particulate processes, where material buildup and solidification are influenced by thermal and chemical interactions [28]. The localized cooling effect creates favorable conditions for this reaction, particularly when combined with the presence of sulfur, which can further harden the formed rings through sulfation. Additionally, the variability in fuel flow introduces dynamic changes in gas composition and temperature, leading to uneven heat distribution along the kiln's length. This, in turn, creates temperature gradients that enhance the tendency for localized cooling and recarbonation, increasing the likelihood of ring formation.

The interplay between fuel variability, sulfur content, and temperature fluctuations highlights the complex nature of ring formation and underscores the importance of stable process control. Reducing fuel flow variability and optimizing gas composition could

minimize these effects, thereby improving temperature stability and reducing ring formation incidents. Further refinement of the model to account for localized thermal and chemical interactions could enhance the predictive capability and provide more targeted recommendations for process adjustments.

5. Conclusions

To gain a deeper understanding of ring formation inside lime kilns, the authors developed a physics-based model to simulate the plant using real operational data, including lime sludge and fuel flows, among other inputs. This paper provides a comprehensive description of the chemical reactions and thermodynamic processes involved in the calcination process.

The developed model follows a finite-dimensional, one-dimensional approach, focusing on longitudinal variation along the kiln. This simplification was necessary to balance accuracy with computational efficiency and to keep simulation times within a reasonable limit. Despite this simplification, the model effectively captures the key dynamics governing ring formation, including the impact of fuel flow fluctuations and sulfur content from NCG. A more detailed thermodynamic analysis of NCG composition, including the varying contributions of individual components (e.g., methanol, sulfur compounds), could improve the model's accuracy in predicting energy fluctuations. However, NCGs originate from various stages of the chemical recovery process, with varying and non-stationary proportions.

The availability of this model creates significant opportunities for conducting multiple simulation tests using input data directly from the plant's instrumentation, either retrospectively or in real-time. In particular, the ability to monitor kiln wall temperatures from the outside could support the development of a digital twin operating in parallel with the real plant. This digital twin would integrate real-time data from sensors (e.g., temperature, pressure, gas composition) with the developed physics-based model, acting as a continuous observer of the system's state.

The digital twin would enable predictive analysis by continuously updating based on plant conditions and identifying patterns linked to ring formation, such as fluctuations in fuel flow and temperature profiles. By providing early warnings and actionable insights, the twin could automate process adjustments (e.g., fuel rate, kiln rotation speed) to stabilize the temperature profile and minimize ring formation. This would support predictive maintenance, reducing unplanned downtime, improving fuel efficiency, and enhancing the overall quality of the lime produced.

Furthermore, the model's adaptability allows it to be refined over time as more data become available, improving its predictive accuracy and operational relevance. Future work could explore extending the model to two or three dimensions to capture radial variations and localized thermal and chemical gradients, further enhancing the understanding and control of ring formation in lime kilns.

Author Contributions: Conceptualization, J.B.; methodology, R.N.-S. and P.P.; software, R.N.-S. and P.P.; validation, R.N.-S., P.P. and J.B.; formal analysis, R.N.-S. and P.P.; investigation, R.N.-S. and P.P.; access to resources, J.B.; writing—original draft preparation, R.N.-S. and P.P.; writing—review and editing, R.N.-S., P.P. and J.B.; project management, P.P.; funding acquisition, J.B. All authors have read and agreed to the published version of the manuscript.

Funding: This research was 100% funded by The Navigator Company, Portugal, and developed under a direct contract with the scientific consultancy company inknow solutions, Portugal.

Data Availability Statement: No further information was required to develop the model presented.

Acknowledgments: The authors want to thank The Navigator Company for their support in the overall project, both financially and for the access to knowledge.

Conflicts of Interest: Author Paulo Pina was employed by the inknow solutions and author Joaquim Belfo was employed by The Navigator Company. The remaining author declare that the research was conducted in the absence of any commercial or financial relationships that could be construed as a potential conflict of interest. The Navigator Company had no role in the design of the study; in the collection, analyses, or interpretation of data; in the writing of the manuscript, or in the decision to publish the results.

Abbreviations

The following abbreviations are used in this manuscript:

CFD	Computational Fluid Dynamics
NCG	Non-Condensable Gas
ODE	Ordinary Differential Equation

References

1. Keim, E.; Zuñiga, J.; Tran, H. Combatting lime kiln ringing problems at the Arauco Constitución mill. *TAPPI J.* **2020**, *19*, 345. [CrossRef]
2. Tran, H.N.; Barham, D. An overview of ring formation in lime kilns. *TAPPI J.* **1991**, *74*, 131–136.
3. Gorog, J.P.; Leary, W. Ring removal in rotary kilns used by the pulp and paper industry. *TAPPI J.* **2016**, *15*, 205–213. [CrossRef]
4. Gareau, P.; Busmann, M.; DeMartini, N.; Tran, H. Effects of rings on flow and temperature in lime kilns. *TAPPI J.* **2022**, *21*, 301. [CrossRef]
5. Rippon, L.D.; Hirtz, B.; Sheehan, C.; Reinheimer, T.; van der Merwe, C.; Loewen, P.; Gopaluni, B. Detection and Diagnosis of Ring Formation in Rotary Lime Kilns. *CSChE Syst. Control Trans.* **2021**, *1*, 23–29.
6. Tran, H.; Mao, X.; Barham, D. Mechanisms of Ringing Formation in Lime Kilns. *J. Pulp Pap. Sci.* **1993**, *19*, 167–175.
7. Lundqvist, P. Mass and Energy Balances Over the Lime Kiln in a Kraft Pulp Mill. Master's Thesis, Uppsala University, Uppsala, Sweden, 2009.
8. Dorris, G.M.; Allen, L.H. The Effect of Reburned Lime Structure on the Rates of Slaking, Causticizing and Lime Mud Settling. *J. Pulp Pap. Sci.* **1985**, *11*, J89–J98.
9. D'Souza, T.; Tran, H.; Repka, J. Effects of Process Variabilty on Ring Formation in Lime Kilns. In Proceedings of the TAPPI Engineering, Pulping and Environmental Conference, Atlanta, Georgia, 5–8 November 2006.
10. Notidis, E.; Tran, H. Survey of lime kiln operation and ringing problem. *TAPPI J.* **1993**, *76*, 125–131.
11. Mohanan, G.; Tran, H.; Bussmann, M.; Manning, R. Effect of ring formation on burner flame stability in lime kilns. *TAPPI J.* **2018**, *17*, 285.
12. Valiquette, J.; Savoie, M.; Leclerc, M. Practical aspects of model predictive control implementation on an industrial lime kiln. In Proceedings of the 1997 European Control Conference (ECC), Brussels, Belgium, 1–7 July 1997. [CrossRef]
13. Juuso, E. Applications of smart adaptive system in pulp and paper industry. In Proceedings of the Symposium on Intelligent Technologies, Hybrid Systems and their implementation on Smart Adaptive Systems, Aachen, Germany, 10–12 June 2004; pp. 21–33.
14. Dhak, J. *Ring Formation in Lime Kilns*; VÄRMEFORSK Service AB: Stockholm, Sweden, 2005. (In Swedish)
15. Rennie, C.; Manning, R.; Cooper, S. Combustion by Design: Optimized Combustion For Lime Recovery Kilns. In Proceedings of the TAPPI International Chemical Recovery Conference, Charleston, SC, USA, 6–10 June 2004.
16. Aloqaily, A.; Kuhn, D.C.S.; Sullivan, P.; Tran, H. Effect of Burning NCG on Lime Kiln Flame Patterns. *J. Pulp Pap. Sci.* **2005**, *31*, 137–142.
17. Biermann, C.J. *Handbook of Pulping and Papermaking*; Academic Press: Cambridge, MA, USA, 1996. [CrossRef]
18. Francey, S.; Tran, H.; Berglin, N. Global survey on lime kiln operation, energy consumption, and alternative fuel usage. *TAPPI J.* **2011**, *19*, 19–26.
19. Lin, B. Collecting and Burning Noncondensible Gases. *TAPPI Kraft Recovery Course* **2007**, *2007*, 295–305.
20. Uronen, P.; Aurasmaa, H. Modelling and simulation of causticization plant and lime kiln. *Pulp Pap. Can.* **1979**, *80*, 162–165.
21. Andreola, R.; Jorge, R.M.; Santos, O. Modeling, Simulation, and Analysis of a Reactor System for the Generation of White Liquor of a Pulp and Paper Industry. *Braz. Arch. Biol. Technol.* **2011**, *54*, 197–206. [CrossRef]
22. Svedin, K.; Ivarsson, C.; Lundborg, R. Lime Kiln Modeling—FCD and One-Dimensional Simulations. 2009. Available online: https://www.osti.gov/etdeweb/servlets/purl/951438 (accessed on 3 October 2023).
23. Ryan, J.; Bussmann, M.; DeMartini, N. CFD Modelling of Calcination in a Rotary Lime Kiln. *Processes* **2022**, *10*, 1516. [CrossRef]

24. Juneja, P.J.; Sunori, S.; Sharma, A.; Sharma, A.; Joshi, V. Modeling control and instrumentation of lime kiln process: A review. In Proceedings of the 2020 International Conference on Advances in Computing Communication & Materials (ICACCM), Dehradun, India, 21–22 August 2020; pp. 399–403.
25. Fardadi, M. Modeling Dust Formation in Lime Kilns. Ph.D. Thesis, University of Toronto, Toronto, ON, Canada, 2010.
26. Paul, M. A Three Dimensional Numerical Model to Predict Temperature and Degree of Calcination in the Solids Bed in Lime Kilns. Master's Dissertation, Department of Chemical Engineering and Applied Chemistry, University of Toronto, Toronto, ON, Canada, 2004.
27. Vakkilainnen, E.K. The Kraft Chemical Recovery Process. 2007. Available online: https://api.semanticscholar.org/CorpusID:15220604 (accessed on 3 October 2023).
28. Lupo, M.; Ajabshir, S.Z.; Sofia, D.; Barletta, D.; Poletto, M. Experimental metrics of the powder layer quality in the selective laser sintering process. *Powder Technol.* **2023**, *419*, 118346.